Journal of Applied Physics

AIP Publishing

A Novel Architecture for room temperature microwave optomechanical experiments

Sumit Kumar,[1] Sebastian Spence,[1] Simon Perrett,[1] Zaynab Tahir,[1] Angadjit Singh,[2] Chichi Qi,[1] Sara Perez Vizan,[1] and Xavier Rojas[1]
[1)]*Department of Physics, Royal Holloway University of London, Egham, Surrey, TW20 0EX, U.K.*
[2)]*Clarendon Laboratory, Department of Physics, University of Oxford, Oxford OX1 3PU, U.K.*

(*Electronic mail: xavier.rojas@rhul.ac.uk)

(Dated: 31 January 2023)

We have developed a novel architecture for room temperature microwave cavity optomechanics, which is based on the coupling of a 3D microwave re-entrant cavity to a compliant membrane. Devices parameters have enabled resolving the thermomechanical motion of the membrane, and observing optomechanically induced transparency/absorption in the linear regime, for the first time in a microwave optomechanical system operated at room temperature. We have extracted the single photon coupling rate (g_0) using four independent measurement techniques, and hence obtain a full characterization of the proposed cavity optomechanical system.

I. INTRODUCTION

The advances in low temperature microwave optomechanics has successfully demonstrated many ground breaking experiments such as ground state cooling[1,2], backaction evading measurements[3,4], entangling massive mechanical resonators[5,6], and ultrasensitive detection of small forces[7,8]. Microwave optomechanical technologies can also foster the architecture for signal processing[9,10] and quantum limited measurements[11,12].

The field of cavity optomechanics has also facilitated many precision sensing applications at room temperature (RT). Schliesser *et al.*[13] achieved the displacement sensitivity of 10^{-19} m/$\sqrt{\text{Hz}}$ by coupling light and mechanical mode of a silica toroidal cavity. Sansa *et al.*[14] demonstrated an optomechanical mass spectrometry able to detect mass up to 100 kDa. Gavartin *et al.*[15] reached a force sensitivity of 74 aN/$\sqrt{\text{Hz}}$ by coupling Si_3N_4 nanomechanical beam to a disk-shaped optical resonator. Other applications include atomic force microscopy[16,17], accelerometry[18], magnetic resonance force microscopy[19]. Fabricating resonators with low mechanical dissipation can also facilitate quantum optomechanical experiments at RT[20]. The above mentioned experiments were all performed at RT in the optical domain. In the microwave domain, there are fewer implementations[21] and their cooperativities are not as high. By optimizing the cooperativity[22] in RT microwave optomechanics, one can further advance the field of ultra-precision sensing and large-scale integration[23].

The cooperativity $C = 4g_0^2 n_\text{d}/(\kappa\Gamma_\text{m})$ characterizes the efficiency of the exchange of photons and phonons in an optomechanical system[24], where g_0 is the single photon coupling rate between the microwave cavity and the mechanical resonators' mode of interest, n_d is the number of the photons inside the cavity, κ and Γ_m are cavity and mechanical resonator decay rates respectively. RT microwave optomechanical experiments have been previously accomplished using microstrip resonators made of normal conducting Cu coupled to a mechanical element[23]. These resonators are marred by dielectric and conductor losses, limiting their quality factor to about 100 which adds a constraint to the displacement and the force sensitivity[25].

One can benefit from coupling mechanical resonators to 3D microwave cavities with low loss. In a recent work by Liu *et al.*[26], backaction evading measurements of a Si_3N_4 membrane resonator was performed via coupling it to a 3D Cu cavity. They observed a cavity quality factor of 15,000 at 300 mK. At low temperatures, the use of high-Q superconducting microwave cavities provided large cooperativities[27] and enabled reaching ground state cooling[28] of a Si_3N_4 membrane. However, above mentioned experiments required low temperatures and an antenna chip to be flip-chip bonded to the Si_3N_4 membrane resonator for microwave coupling, increasing fabrication steps. Tuan *et al.*[25] also employed a 3D microwave cavity made of Cu to dielectrically couple to a Si_3N_4 string. They characterized the optomechanical coupling by driving the string using two tones in a nonlinear regime at RT.

Here, we present a novel architecture for RT microwave optomechanics. Our cavity optomechanical system is composed of a Si_3N_4 membrane coupled to a 3D microwave re-entrant cavity. Our relatively high cooperativity for a microwave optomechanical system enables detecting thermomechanical motion and optomechanically induced transparency/absorption (OMIT/OMIA) with great resolution. Using four independent characterization techniques, we extract the single photon coupling rate g_0, a key metric for cavity optomechanical systems. We pushed this system into the nonlinear regime to extract the duffing parameter, hence defining the dynamic range for sensing applications.

II. OPTOMECHANICAL SYSTEM

The cavity optomechanical systems consist of a Si_3N_4 membrane coupled to a 3D microwave cavity. The microwave re-entrant cavity consists of a post enclosed in a cylindrical cavity leaving a tiny gap between the top of the post and a cavity wall, as shown in Fig. 1. The cavity is made of Cu which is electropolished[29] and gold plated[30]. The electric field of the

fundamental electromagnetic mode within is highly confined within the gap between the top of the post and the wall of the lid, which for this experiment is a window to a gold plated Si_3N_4 membrane, as shown in Fig. 1.

The resonance frequency of the cavity is given by $\omega_c = 1/\sqrt{LC}$. The capacitance $C = C_0 + C_1$ where C_0 is the capacitance between the top of the post and the wall of the lid determined by the gap and C_1 is the capacitance of the rest of the cavity. The inductance L is defined by the geometry of the post inside the cavity. Any change in the gap will be translated to a change in the resonance frequency of the cavity. Thus, if the end wall is made of any mechanical resonator, the system behaves as a transducer for detecting mechanical motion. We incorporated a 5 mm $\times$ 5 mm chip with a mechanical resonator within a window in the lid. The chip is placed across the window from the reverse side of the lid and secured in place with a PTFE grub screw.

The mechanical resonator is a 2 mm $\times$ 2 mm prestressed Si_3N_4 membrane[31]. The Si_3N_4 membrane is 50 nm thick, plated with 55 nm of Au. The motion of the mechanical resonator will thus induce modulation of the resonance frequency of the cavity owing to a change in the gap. The optomechanical coupling strength $G = \partial\omega_c/\partial x$ is inversely proportional to the gap x. We targeted the gap to be $x \sim 100\ \mu$m when machining the cavity. We then estimated the gap to be close to $x \sim 100\ \mu$m (see Appendix A) by comparison with the analytical expression for the resonance frequency of the re-entrant cavity and the FEM simulation using COMSOL. We attached a piezo-electric transducer (PZT) to the cavity lid. The cavity is placed inside a vacuum chamber with pressure below 5×10^{-6} mbar. All the measurements were performed at room temperature.

III. CHARACTERIZATION

The two-port microwave cavity is characterized via the measurement of scattering parameters with a vector network analyzer (VNA). The external microwave feedlines are capacitively coupled to the cavity using SMA pins. The length these pins protrude into the cavity determines the coupling strength κ^1_{ext} and κ^2_{ext} of port 1 and port 2, respectively. The dielectric and conductor losses are characterized by κ_{int} such that the total loss in the cavity is $\kappa = \kappa^1_{ext} + \kappa^2_{ext} + \kappa_{int}$. From our measurements, the resonance frequency of the cavity is $\omega_c/(2\pi)$= 4.537 GHz, the linewidth is $\kappa/(2\pi)$= 5.504 MHz, and external linewidths are $\kappa^1_{ext}/(2\pi)$=$\kappa^2_{ext}/(2\pi) \approx 245$ kHz. The amplitude $|S_{21}|$ is plotted in the Fig. 2. The quality factor of the cavity is 800 and the coupling efficiency is κ^1_{ext}/κ= 0.044, showing the cavity is under-coupled. The quality factor can be further increased by the surface treatment of Cu.

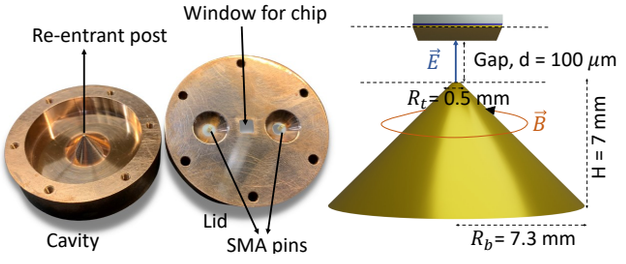

FIG. 1. (left) The cavity with chip window and SMA pin couplers. (right) Schematic of the re-entrant pillar and Si_3N_4 membrane chip. The cylindrical cavity with an inner radius of $R_{cav} = 18$ mm with a conical post of height $H = 7$ mm, bottom radius $R_b = 7.3$ mm and top radius $R_t = 0.5$ mm constitutes our 3D cavity. The electric field of the fundamental mode of the cavity is confined between the chip and the top of the post whereas the magnetic field is around the post.

The characteristics of the fundamental mode of the mechanical resonator and the single photon optomechanical strength g_0 were extracted using four different methods. Firstly, we measured the thermomechanical motion by driving the cavity at its resonance frequency ω_c and measuring the noise spectrum at $\omega_c + \Omega_m$ where Ω_m is the resonance frequency of the fundamental mode of the mechanical resonator using the spectrum analyzer. Secondly, we again measured the noise spectrum at $\omega_c + \Omega_m$ by driving the cavity at ω_c and the mechanical resonator using white noise imparted by the PZT. Thirdly, we characterized g_0 using two tone measurements thus demonstrating OMIT/OMIA in the response of the cavity and at last, we employed a homodyne detection scheme to extract g_0. Finally, we study the mechanical resonator in the nonlinear regime to extract the duffing parameter, and hence quantify the dynamic range for potential sensing applications.

A. Thermal noise measurement

The motion of the mechanical resonator with resonance frequency Ω_m will modulate the cavity drive frequency ω_d generating sidebands at $\omega_d \pm \Omega_m$. The thermomechanical motion of the Si_3N_4 membrane was measured by applying a microwave signal to port 1 of the cavity at ω_d and measuring the noise spectrum of the transmitted signal at $\omega_d + \Omega_m$ using a spectrum analyzer. The loss and gain contributions of the input and the output lines were removed via careful calibrations. The measurement circuit diagram is described in appendix C. We focus on the fundamental flexural mode with resonance frequency Ω_{11} of the Si_3N_4 membrane. Theoretically, the resonance frequency Ω_{11} can be determined using the square membrane formula[32],

$$\frac{\Omega_{11}}{2\pi} = \frac{1}{2}\sqrt{\frac{\sigma}{\rho}\frac{2}{a^2}}\,, \tag{1}$$

where $\sigma = 1$ GPa is the stress in the Si_3N_4 membrane (information provided by the supplier Norcada Inc.[31]), $\rho = 2820 \pm 160$ kg/m^3 is the mass density of the Si_3N_4, and $a = 2$ mm is its lateral dimension. However, the resonance frequency changes due to the loaded mass of 55 nm Au on the membrane. The modified resonance frequency Ω_m is given by[33],

$$\Omega_m = \sqrt{\frac{m_{eff,11}\Omega_{11}^2}{m_{eff,11} + m_{load}}}\,, \tag{2}$$

where $m_{\mathrm{eff},11}$ is the effective mass of the fundamental flexural mode of Si_3N_4 membrane and m_{load} is the effective mass of the loaded Au on Si_3N_4 membrane. Theoretically, $\Omega_{\mathrm{m}}/(2\pi) = 72$ kHz. The cavity mode is pumped by applying a microwave signal ω_{d}. We also define a detuning $\Delta = \omega_{\mathrm{d}} - \omega_{\mathrm{c}}$. For in-cavity pumping, the number of drive photons n_{d} inside the cavity is given by[34],

$$n_{\mathrm{d}} = \frac{2\kappa_{\mathrm{ext}} P_{\mathrm{in}}}{\hbar\omega_{\mathrm{c}}(\kappa^2 + 4\Delta^2)}\,, \tag{3}$$

where $\kappa_{\mathrm{ext}} = \kappa^1_{\mathrm{ext}} + \kappa^2_{\mathrm{ext}}$ and P_{in} is the power incident on port 1. The power spectral density, $S[\Omega]$ (W/Hz) at $\omega_{\mathrm{d}} + \Omega_{\mathrm{m}}$ coming out of port 2 of the cavity in the frame rotating with ω_{c} is given by[34,35],

$$S[\Omega](\mathrm{W/Hz}) = \frac{\kappa_{\mathrm{ext}} G^2 n_{\mathrm{d}}}{\kappa^2}\hbar\omega_{\mathrm{c}} S_x[\Omega] + \mathrm{nf}\,, \tag{4}$$

where nf is the noise floor and $S_{\mathrm{x}}[\Omega]$ is given by,

$$S_x[\Omega](\mathrm{m^2/Hz}) = \frac{4k_{\mathrm{b}}T}{m_{\mathrm{eff}}\Omega_{\mathrm{m}}^2}\frac{\Gamma_{\mathrm{m}}}{\Gamma_{\mathrm{m}}^2 + 4(\Omega - \Omega_{\mathrm{m}})^2}\,, \tag{5}$$

is the single-sided noise position spectral density[36]. k_{b} is the Boltzmann's constant, $T = 293$ K, Γ_{m} is the mechanical linewidth, x is the global RMS displacement of the Si_3N_4 membrane normalized by mode shape function at temperature T and Ω is close to Ω_{m}. The power spectral density at $\Delta + \Omega_{\mathrm{m}}$ is plotted in Fig. 2. From a Lorentzian fit of the experimental data, we extracted $\Omega_{\mathrm{m}}/(2\pi) = 71.4$ kHz and $\Gamma_{\mathrm{m}}/(2\pi) = 8.4$ Hz, giving rise to the mechanical quality factor Q of 8500.

Next, we focused on extracting single-photon coupling rate $g_0 = Gx_{\mathrm{zpf}}$, where $x_{\mathrm{zpf}} = \sqrt{\hbar/(2m_{\mathrm{eff}}\Omega_{\mathrm{m}})}$ is the zero-point fluctuation of the mechanical mode and $m_{\mathrm{eff}} = m_{\mathrm{eff},11} + m_{\mathrm{load}}$ = 1.20 ng giving $x_{\mathrm{zpf}} = 0.31$ fm. The noise floor nf is subtracted from the power spectral density S such that $S - \mathrm{nf}$ is written in terms of position spectral density S_x. We then fitted the resultant plot using Eqs. 4 and 5. If we take the theoretical value of m_{eff} and x_{zpf}, only g_0 remains unknown. From the fit, we extracted $g_0/2\pi = Gx_{\mathrm{zpf}}/2\pi = 185\pm11.5$ μHz.

The noise floor in our detection signal corresponds to a displacement sensitivity of 0.75 pm/$\sqrt{\mathrm{Hz}}$. This represents approximately an order of magnitude improvement from previously reported displacement sensitivity[23].

B. White noise drive

Extracting g_0 is usually a difficult task unless one can directly measure the thermal motional sidebands as described in the previous section. In some cases, there is not enough sensitivity to detect the thermal motion of the mechanical resonator. One can therefore drive the mechanical system with an external force as the one generated from, for instance, a piezoelectric transducer. However, it is difficult to know precisely the conversion factor between the voltage applied across the piezoelectric transducer and the force generated on the mechanical resonator, hence preventing the derivation of g_0. Instead, the technique we present now uses a source of white noise to drive the piezoelectric transducer, generating a noise force on the mechanical resonator. This increases the effective mode temperature and the amplitude of the mechanical sideband measured at $\Delta + \Omega_{\mathrm{m}}$. Fig. 3 shows the mechanical sideband at $\Delta + \Omega_{\mathrm{m}}$ when the cavity is pumped at ω_{c} for different RMS voltages of white noise applied to the transducer. One can see roughly two orders of magnitude of increase in the amplitude of the mechanical sideband when driven by 1000 $\mu\mathrm{V}^2/\mathrm{Hz}$ of white noise generated by the noise source in the bandwidth of 10 MHz compared to the undriven case. From Eq. 4, the area under the power spectral density is directly proportional to the temperature bath. We subtract the nf from the measured spectral density $S[\Omega]$ and integrate the curve in the bandwidth of 500 Hz, to calculate the area under the power spectral density. The area calculated for each PZT drive was normalized by area in the case of undriven PZT, to calculate the effective temperature of the mechanical mode. From this, an effective temperature of $\sim$ 23,000 K was found at 1000 $\mu\mathrm{V}^2/\mathrm{Hz}$ of white noise. The effective temperature varies linearly with the area under the power spectral density and is plotted in Fig. 3. For comparison, a value of g_0 can be obtained by extracting the slope from the linear fit. The slope ζ is given by,

$$\zeta = \frac{m_{\mathrm{eff}}\Omega_{\mathrm{m}}^2\kappa^2}{2\pi\kappa_{\mathrm{ext}}G^2 n_{\mathrm{d}}\hbar\omega_{\mathrm{c}}k_{\mathrm{b}}} \tag{6}$$

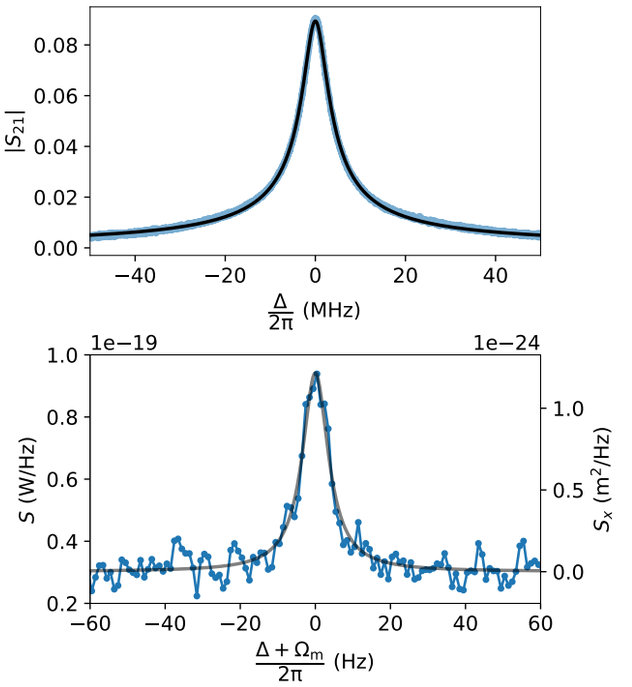

FIG. 2. (top) The transmission S_{21} is plotted for the microwave cavity. (bottom) Noise power spectral density of mechanical sideband at $\Delta + \Omega_{\mathrm{m}}$ due to brownian motion of Si_3N_4 membrane with $n_{\mathrm{d}} = 3.6 \times 10^{11}$ for -6.8±0.5 dBm of input power to port 1 of the cavity. For both plots, experimental data is shown in blue and the fits are in grey. The noise floor has been subtracted on the right scale.

We put the value of slope ζ into equation 6 giving $g_0/2\pi = 185\pm11.5$ μHz for this method consistent with the previously derived value.

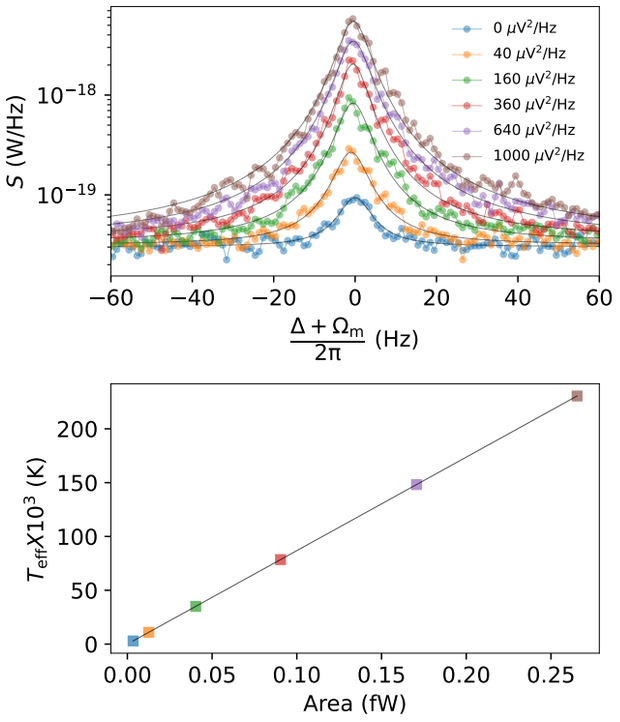

FIG. 3. (top) The power spectral density of mechanical sideband at $\omega_c + \Omega_m$ is plotted for different values of white noise voltage applied across the piezoelectric transducer. The fits are shown in grey. We have used the blue curve data, where the mechanical mode is assumed to be in thermal equilibrium, as calibration to calculate the effective temperature of other curves. (bottom) The effective temperature is plotted versus the area under power spectral density for each noise voltage drive used in the top figure (same color coding). The slope ζ of the linear data is used in Eq. 6 to extract g_0.

C. OMIT/OMIA

OMIT/OMIA is the optomechanical analog of electromagnetically induced transparency observed in cold atoms[37]. It was theoretically predicted[38] in 2009 and first observed in optical systems[39,40]. Exploiting this effect could be useful to signal processing applications such as delay lines or memories. Here we present the first measurement of OMIT/OMIA in a microwave cavity optomechanical system operated at room temperature. This measurement also enables us to extract g_0 with an additional independent characterization technique.

The cavity is driven by a strong pump at $\omega_d = \omega_c + \Delta$ and is probed with a relatively weaker signal at ω_p resulting in the radiation pressure force on the mechanical resonator at the difference frequency $\Omega = \omega_p - \omega_d$. The mechanics is coherently driven when $||\Omega| - \Omega_m| \lesssim \Gamma_m$. The driven mechanics generates sidebands on the pump tone. The sideband then interferes constructively or destructively with the probe tone, depending on the sign of Δ, where $\Delta = \pm\Omega_m$, thus influencing the cavity transmission. When $\Delta = -\Omega_m$ (red pump), the sideband generated at ω_c interferes destructively with ω_p leading to OMIA. On the other hand, a transparent window is opened at ω_c (OMIT) when probing cavity transmission when $\Delta = \Omega_m$.

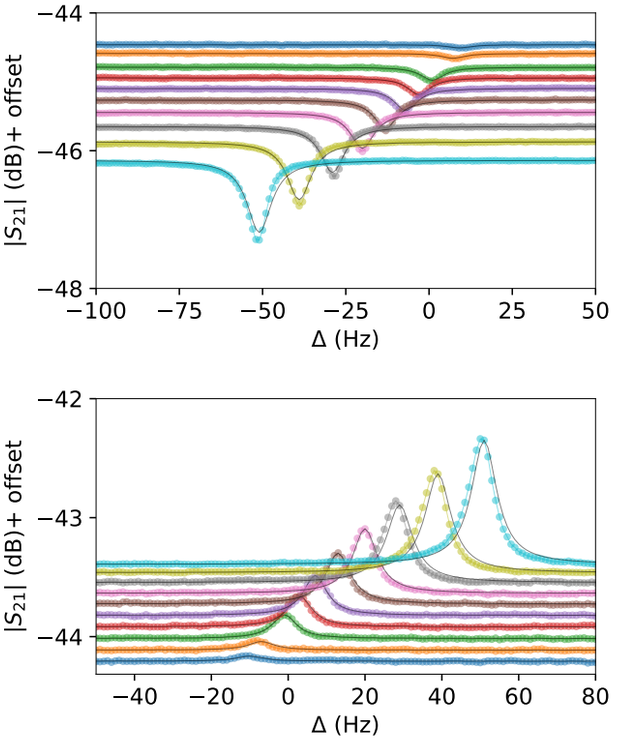

FIG. 4. (top) OMIA was observed in the vicinity of ω_c when pump tone is applied at $\omega_c - \Omega_m$. The number of photons n_d was varied from 1.7 $\times 10^{12}$ (blue curve) to 3.8 $\times 10^{13}$ (cyan curve). Grey lines are the fits. (bottom) OMIT was observed when pump tone was applied at $\omega_c + \Omega_m$. All the parameters are the same as the top plot. There is an offset in the y-axis for both plots for clarity.

The circuit diagram for the measurement is discussed in appendix C. Fig. 4 (top) shows the OMIA response while using red pump tone at $\omega_c - \Omega_m$. The drive photons n_d were varied from 1.7×10^{12} to 3.8×10^{13} photons. The weaker probe tone ω_p with -40 dBm of power applied by the source was swept in a narrow window of 200 Hz about ω_c. Increasing the number of drive photons led to stronger driving of the mechanical resonator, thus increasing the amplitude of the absorption curve. Ideally, the absorption curves should be at ω_c, but we observed a frequency shift in the absorption curves as we increased the number of photons shown in Fig. 4. The y-axis in Fig. 4 is also offset for clarity. We observe a spring softening caused by the pump signal, which corresponds to a temperature elevation of the membrane of the order of 2 K at the maximum power. More information on this effect can be found in the

appendix B. The transmission $S_{21}[\omega_p]$ is given by[9],

$$S_{21}[\omega_p] = 1 - \frac{\chi_c[\omega_p]\kappa_{ext}/2}{1 \mp g_0^2 n_d \chi_c[\omega_p]\chi_m[\omega_p]}, \tag{7}$$

where $\chi_c^{-1}[\omega_p] = \frac{\kappa}{2} - i(\Omega + \Delta)$ and $\chi_m^{-1}[\omega_p] = \frac{\Gamma_m}{2} - i(\Omega \pm \Omega_m)$. The upper (lower) sign in $S_{21}[\omega_p]$ and $\chi^{-1}[\omega_p]$ is for blue (red) pumping. Eq. 7 was used to fit the curves in Fig. 4 extracting $g_0/(2\pi)$ = 192 ± 12 μHz, consistent within $\sim$ 5% of g_0 derived from direct power spectral density measurements detailed in subsection III A. Similar measurements were made with blue pump at $\omega_c + \Omega_p$, finding a similar value of g_0 and we observing OMIT shown in Fig. 4 (bottom).

IV. HOMODYNE DETECTION

An alternative to direct detection with a spectrum analyzer is the homodyne detection method. A microwave interferometer type method, downconverting the signal at $\omega_d + \Omega_m$ by mixing with a local oscillator signal at ω_d to generate a signal at Ω_m, measured by a lockin amplifier (see Fig. 9). Here, $\omega_d = \omega_c$ is at the microwave resonance frequency, for a phase-sensitive measurement with maximum sensitivity. We measure the voltage spectral density $S_V[\Omega]$ of the signal at Ω_m using zoom fast fourier transformation, where the signal at Ω_m is downmixed with a signal near Ω_m, greatly increasing measurement speed. The voltage spectral density is given by,

$$S_V[\Omega](V^2/Hz) = \frac{K\kappa_{ext}G^2 n_d}{\kappa^2}\hbar\omega_c S_x[\Omega] + nf, \tag{8}$$

where K is a scaling factor that depends on the input impedance of the lockin amplifier, attenuation in the circuit, and the phase difference of the microwave pump signal ω_d in different parts of the circuit. The square root of the area under the position spectral density $S_x[\Omega]$ shown in Fig. 2 gives the normalized RMS mechanical amplitude $x_{RMS} = \sqrt{\langle x \rangle^2} =$ 4 pm. The square root of the area under $S_V - nf$ at Ω_m is the RMS voltage V_{RMS} measured by the lockin amplifier such that

$$V_{RMS} = \sqrt{\frac{K\kappa_{ext}G^2 n_d}{\kappa^2}\hbar\omega_c}\, x_{RMS.} \tag{9}$$

We subtracted the noise floor nf from S_V and calculated the square root of the area under the curve giving $V_{RMS} = 0.1\ \mu V$. Putting the value $x_{RMS} = 4$ pm in Eq. 9, we extracted

$$K_1 = \sqrt{\frac{K\kappa_{ext}G^2 n_d}{\kappa^2}\hbar\omega_c} = 4 \times 10^4, \tag{10}$$

where K_1 is the scaling factor to convert V_{RMS} measured by the lockin to the RMS displacement x_{RMS} of the mechanical resonator. By applying an AC electrical signal on the PZT at Ω it will then impart a sinusoidal force at Ω to the mechanical resonator, driving it coherently. The measurement circuit is shown in appendix C. The eigenfrequencies of the mechanical resonator were characterized by sweeping Ω from 50 kHz to 400 kHz, and measuring the response at the lock-in at the swept frequency. The different eigenmodes are shown in Fig. 5. The eigenfrequencies of different modes match with the theoretical values within 1 %. Ideally, degenerate pairs of modes like (2,3),(3,2); (1,6),(6,1), etc. should have identical eigenfrequencies, but we observed a mismatch shown in the inset of Fig. 5. This mismatch can be attributed to the unsymmetrical edges of the square membrane.

Characterizing nonlinearity in the mechanical resonator is also an important step with its applications in signal processing and precision sensing[41]. For this characterization, we measured the response of the fundamental mode (1,1) of the Si_3N_4 membrane. The PZT was driven by an upward-sweeping sinusoidal signal across the mechanical resonance. The response of the mechanical resonator can be modeled using a duffing non-linear equation of motion,

$$\frac{\partial^2 x}{\partial t^2} + \Gamma_m \frac{\partial x}{\partial t} + \Omega_m^2 x + \alpha x^3 = \frac{F\cos(\Omega t)}{m_{eff,11}} \tag{11}$$

where x is the mechanical displacement, α is the duffing parameter. The drive voltage applied to the PZT varied from 10 mV_{RMS} to 900 mV_{RMS}. The response of the mechanical resonator is shown in Fig. 5. For weaker drives, the response of the mechanical resonator is Lorentzian around the resonance frequency Ω_m. Increasing the drive voltage, the maximum amplitude x_{max} shifts to higher frequencies Ω_{eff} visible in Fig. 5. This behavior is well approximated by the backbone curve equation as[41],

$$x_{max}^2 = \frac{8}{3}\frac{\Omega_m}{\alpha}(\Omega_{eff} - \Omega_m) \tag{12}$$

Using the above equation we extracted the duffing parameter $\alpha = 1.68 \times 10^{19}$ m^{-2} s^{-2}. We also theoretically determined the duffing parameter using the expression given by Cattiaux *et al.*[42] and found it to be 4.2 $\times 10^{19}$ m^{-2} s^{-2} which closely matches with the experimental value. In conclusion, with this architecture, we can probe a displacement amplitude from 4 pm to 100 nm in the linear regime, up to hundreds of nm, and more in the non-linear regime.

A. Calibrated Homodyne

We have used the phase-sensitive homodyne detection technique to measure the optomechanical sidebands of the membrane-cavity system. However, to calculate a g_0 using this technique a calibration of the circuit is required. We wish to avoid a direct calibration of the greater microwave circuit's transmission, which will slowly drift. Instead, we create a reference sideband by phase modulating the source's microwave signal, at ω_d, by a known magnitude ϕ_{mod} and frequency Ω_{mod}, close to Ω_m. This method follows the methodology of Ref.[43], but is adapted from optics to microwaves using phase noise measurement techniques[44]. Following Ref.[43] we derive an equation for the vacuum optomechanical coupling

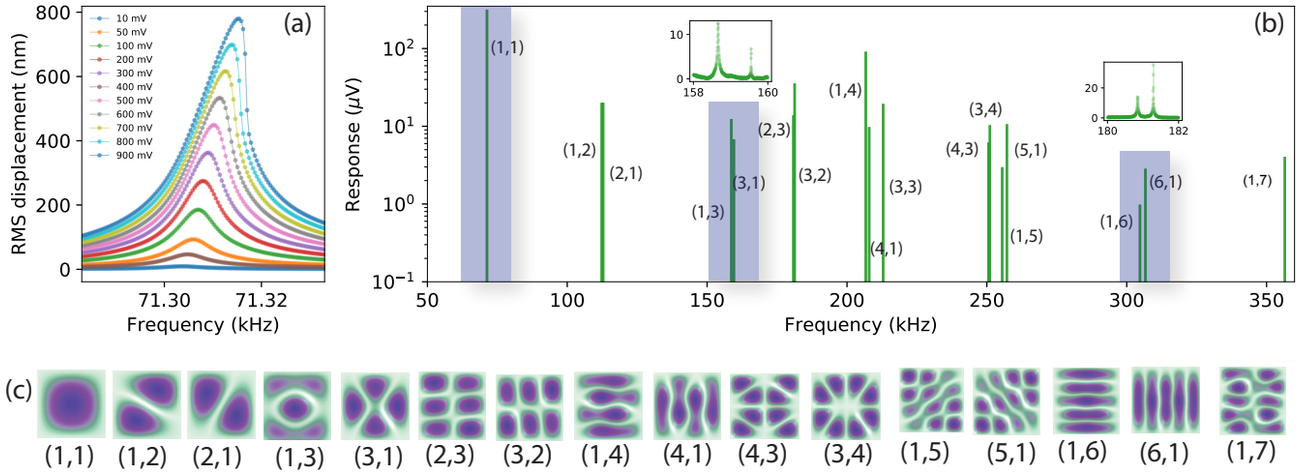

FIG. 5. (a) Nonlinearity observed in mode (1,1) of the membrane by increasing the drive voltage from 10 mV_{RMS} to 900 mV_{RMS}. b) Different eigenmodes of Si_3N_4 membrane resonator detected by sweeping the drive frequency Ω from 50 kHz to 400 kHz. c) Mode shapes for different eigenmodes of the membrane. Dark blue color shows the region of maximum amplitude and light green is the region of minimum amplitude.

in the strong sideband unresolved regime,

$$g_0^2 = [\kappa_L \phi_{mod} \sin(\psi_r/2)]^2 \frac{\Gamma_m S_V[\Omega_m]}{16BW\langle n_m\rangle S_V[\Omega_{mod}]}, \qquad (13)$$

where ψ_r is the relative phase difference between the two arms of the circuit, BW is the bandwidth of the lock-in measurement, and $\langle n_m\rangle$ is the average occupation of the mechanical mode. Then $S_V[\Omega_m]$ and $S_V[\Omega_{mod}]$ are the peak voltage noise values of the optomechanical and modulated signal respectively, as measured by the lock-in. ψ_r is approximately the product of the relative microwave time delay τ_r between the two arms and Ω_m, for our measurement setup this is calculated to be $\psi_r = 0.686$ mrad. In an earlier experiment, we used this technique to measure a coupling for the same membrane-cavity system of $g_0/(2\pi) = 115$ μHz, with the reduced value likely from an unoptimized microwave cavity coupling leading to a reduction in sensitivity. Though this method requires additional setup, it does eliminate the need for sensitive microwave detection equipment.

V. CONCLUSIONS

To summarize, we have demonstrated a cavity optomechanical system realized using a prestressed Si_3N_4 membrane coupled to a re-entrant microwave cavity made of Cu. Our microwave optomechanical setup is capable of resolving the thermomechanical motion of the Si_3N_4 membrane at RT. Moreover, the PZT attached to our setup helped us to excite different mechanical modes of the membrane and also deduce the geometric non-linearity. We extracted the average single photon coupling rate $g_0/(2\pi) = 188.5 \pm 11.5$ μHz for the fundamental mode using direct spectral and two tone measurements and cooperativity of $C = 4g_0^2 n_d/(\kappa\Gamma_m) = 1.2 \times 10^{-3}$ at the maximum pump power used which is close to 13 dBm going into the cavity. The dynamic optomechanical effects such as cooling and heating of the mechanical mode are within our reach just by improving upon the architecture of our setup. By precision machining of our cavity, we can further reduce the gap between the membrane and the top of the pillar of the cavity to less than 10 μm, leading to 10 times increase in g_0, therefore reaching the self-oscillation regime with $n_d \sim 10^{14}$ in the cavity at RT. Further, we can develop microwave notch filters and amplifiers using OMIT/OMIA. Using a strong pump tone at $\omega_d = \omega_c + \Delta$ with $\Delta = \Omega_m$ and using a weaker probe tone at ω_p to sweep the response of the cavity, we can achieve a gain at ω_c close to 25 dB with $n_d \sim 10^{12}$ in the cavity with the gap $x \sim 10$ μm. This magnitude of gain at RT is comparable to similar measurements made at cryogenic temperatures[10]. On the other hand, notch filters can be realized using the two tone measurement but with $\Delta = -\Omega_m$. The novelty of our microwave optomechanical system working at RT and the prospects of making amplifiers, filters and notch filters with performances similar to the systems working at cryogenic temperatures are exciting and are within our reach. Recently, Serra *et al.*[22] mentioned the importance of isolating the mechanical resonator from the substrate to improve the quality factor and a step towards room temperature quantum optomechanics. Our system is flexible to quickly test different kinds of mechanical resonators (trampoline, phononic crytals, Si_3N_4 membranes with soft clamping, etc.). Also, using the two pillars inside the cavity[45] and coupling them to two or more mechanical resonators, which our system is capable of, provides an ideal platform for multimode optomechanics.

ACKNOWLEDGMENTS

This research is supported by the Royal Society (UF150140, RGF\EA\180099, RGF\R1\180059, RGF\EA\201047, RPG\2016\186, URF\R\211009), the EPSRC (EP/R04533X/1), and the STFC (ST/T005998/1). For the purpose of open access, the author has applied a Creative Commons Attribution (CC BY) licence (where permitted by UKRI, 'Open Government Licence' or 'Creative Commons Attribution No-derivatives (CC BY-ND) licence' may be stated instead) to any Author Accepted Manuscript version arising.

DATA AVAILABILITY

The data that support the findings of this study are openly available at https://doi.org/10.5281/zenodo.7589222, Ref.[46].

Appendix A: Estimating gap between re-entrant post and the Si_3N_4 membrane

The microwave cavity is designed with a cone-shaped pillar inside it. The cavity of radii $R_{cav} = 18$ mm and height $H = 7$ mm consists of a cone-shaped pillar with a top radius of 0.5 mm and the bottom radii of 7.3 mm shown in Fig. 6. The resonance frequency of the microwave cavity primarily depends on the gap between the top part of the cone and the chip. We performed FEM simulation using COMSOL shown in Fig. 6 to extract the microwave resonance frequency. With a gap of 100 μm between the lid/chip and the top radii of the cone, the simulated resonance frequency of 4.62 GHz matches with the experimental value of the resonance frequency within 1 %.

Appendix B: Spring softening of Si_3N_4 membranes

In subsection III C, we discussed the spring softening of the Si_3N_4 membrane. We observed a decrease in the resonance frequency of the mechanical mode associated with an increase in the applied pump power. The magnitude of the frequency shift is of the order of 50 Hz at the maximum input power used in this experiment (13.5 dBm). This is observed at zero detuning ($\omega_d = \omega_c$), and for both blue detuned ($\omega_d = \omega_c + \Omega_m$) and red detuned ($\omega_d = \omega_c - \Omega_m$) pumps. In the strongly unresolved sideband regime ($\kappa >> \omega_m$), the drive photon number is nearly the same in all three cases (green, blue and red pumping). At the highest input power P_{in} =13.5 dBm (0.022 W), the drive photon number in the cavity is $n_d = 3.8 \times 10^{13}$. Hence, the total power dissipated by the cavity is given by

$$P_{diss} = (\hbar\omega_d) n_d \kappa_{int} \simeq 4 \text{ mW} \qquad \text{(B1)}$$

with $\kappa_{int} = \kappa - \kappa_{ext} = (2\pi) \times 5.502$ MHz. We note that the internal cavity loss has a contribution to the electrical resistance of the thin gold layer coating of the chip. Hence, a fraction

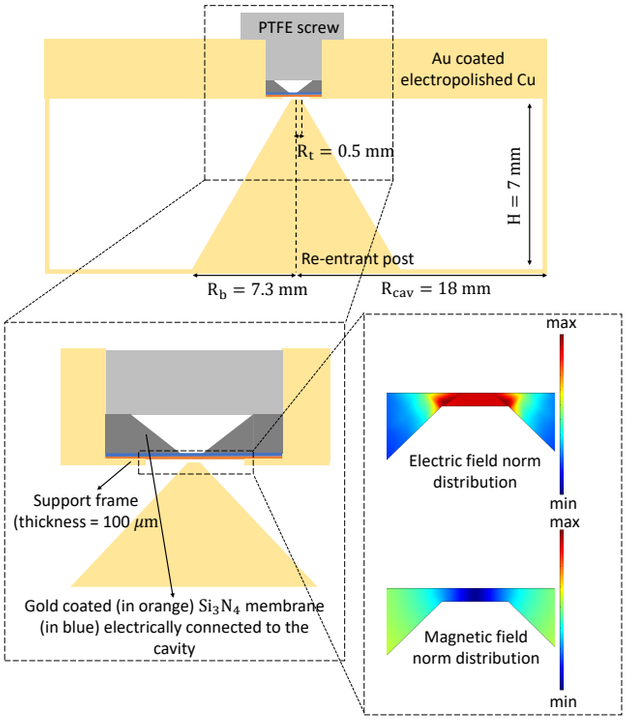

FIG. 6. (top) Figure showing the dimensions of the simulated re-entrant cavity and the (bottom left) zoomed schematic showing the positioning of the chip and PTFE screw clamping it, (bottom right) FEM simulation of the re-entrant cavity where the color scale indicates the magnitude of the electric field in the cavity. The resonance frequency predicted by simulation is 4.62 GHz.

of the electrical power is dissipated in the vicinity of the chip, which can cause local heating of the membrane.

Using COMSOL, we showed in a simple 2D FEM simulation, that a local heating effect of the membrane corresponding to a fraction of the total dissipated power, of the order of a percent, can explain on an average temperature elevation of the membrane $\Delta T = 2$ K. In this model, we considered a 2 $\times$ 2 mm free-standing Si_3N_4 membrane, and assumed a perfect thermalization of the membrane's boundary at the ambient room's temperature. Fig.7 shows the membrane's temperature profile.

Because of thermal expansion, the membrane's temperature elevation causes a resonant mode frequency shift. Using the expression given by Zhang *et al.*[47]

$$\Delta f \approx -\frac{\alpha E f_{11}}{2\sigma(1-\nu)} \Delta T_m \,, \qquad \text{(B2)}$$

one can calculate the frequency shift Δf, where $\alpha = 2.2 \times 10^{-6}$ K^{-1} is the thermal expansion coefficient, $E = 250$ GPa[31] is Young's modulus, $\sigma = 1$ GPa[31] is the in-built stress and $\nu = 0.23$ is the Poisson's ratio of the Si_3N_4 membrane. The frequency shift calculated using this model is consistent with a power absorbed by the membrane of the order of 1% of the total dissipated power, which seems realistic. An in-depth description of this thermal heating effect would fall outside the

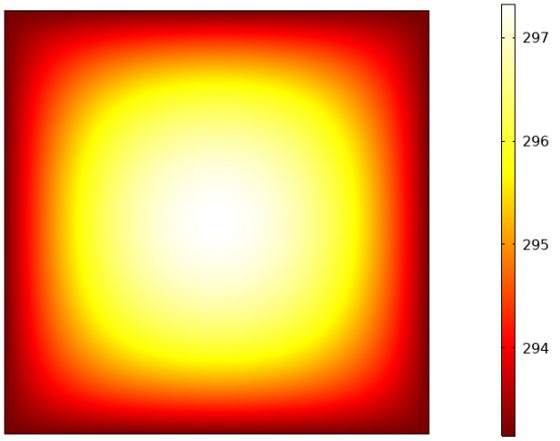

FIG. 7. (top) 2D FEM simulation using COMSOL showing the temperature map of 2 mm $\times$ 2 mm Si_3N_4 membrane. The boundaries are acting as heat sink at RT.

scope of this paper.

Appendix C: Circuit diagrams

This appendix will discuss the circuit diagrams used for each distinct measurement. Fig. 8 shows the circuit diagram for thermal noise measurements, white noise drive measurements, and OMIT/OMIA.

1. Thermal noise measurements

For the thermal noise measurements, the PZT drive and probe tone were off. The microwave pump signal at ω_d generated by the microwave source (Rohde and Schwarz SMF 100A signal generator) was fed to the re-entrant cavity via port 1 shown in shaded light yellow in Fig. 8. The re-entrant cavity can be modeled as a parallel RLC circuit. The capacitance C_0 between the end post and the mechanically compliant Si_3N_4 membrane resonator is then varied by the oscillations of the membrane. Due to the thermomechanical motion of the mechanical resonator with resonance frequency Ω_m, the signal at ω_d is modulated such that the signal coming out of the cavity from port 2 has three frequency components (ω_d, $\omega_d + \Omega_m$, $\omega_d - \Omega_m$). We cancel the signal coming out of port 2 at ω_d by combining it with another signal at ω_d by adjusting the phase shifter (Pasternack Phase shifter) (ϕ) and the variable attenuator (Mini-Circuits digitally controlled variable attenuator). The signal is then amplified using a room temperature amplifier (LNF RT HEMT, 4 GHz-12 GHz) before measuring the noise using the spectrum analyzer (Rohde and Schwarz SMF Signal and Spectrum Analyzer). The pump tone was applied at the microwave resonance frequency such that $\omega_d = \omega_c$, where ω_c is the microwave resonance frequency. We used 5 dBm of input power from the generator, which was further attenuated by power dividers and coaxial lines such that the power reaching the input port of the cavity was -6.8 dBm which was measured using a Keysight microwave power meter. The gain in the circuit was 23.5 dBm. We then measured the signal at $\omega_c + \Omega_m$ using the spectrum analyzer.

2. White noise driven spectral measurements

For the white noise driven Si_3N_4 membrane, the piezoelectric transducer was excited by white noise in the bandwidth of 10 MHz using function generator (Stanford SRS DS345), keeping every element of the circuit the same as in the thermal noise measurements. The signal was measured using the spectrum analyzer.

3. Two-tone measurements

When measuring the transmission of the cavity using two tone, the PZT drive was turned off. The pump tone at ω_d was combined with a weaker probe tone at ω_p generated by another microwave source (Rohde and Schwarz SMP 22 Signal generator) before the signal was fed to the microwave cavity. The pump tone at ω_d was kept fixed such at $\Delta = \omega_d - \omega_c$. The weaker probe tone with power of -40 dBm at ω_p was swept from $\omega_c - 200\pi$ to $\omega_c + 200\pi$. The pump tone power generated by the source was also varied from 16 dBm to 25 dBm.

4. Homodyne detection

For the homodyne detection scheme, we use a lockin amplifier to detect the signal. The microwave pump at ω_d was again fed to the re-entrant cavity via port 1 as shown in Fig. 9. In the case of driven periodic motion of the membrane by exciting the PZT at RF frequency Ω generates sidebands on the pump signal at $\omega_d \pm \Omega$. The transmitted signal is amplified using an RT microwave amplifier (Mini-circuits microwave amplifier, 4 GHz-12 GHz). The amplified signal is then mixed with a microwave signal at ω_d such that the signal coming out of the mixer is at $\pm\Omega$. We cancel the DC component by adjusting the phase shifter also shown in Fig. 9. The RF signal is filtered removing any high frequency component before being measured by the lockin amplifier (Zurich Instrument, HF2LI). The RF signal Ω driving the PZT is swept across the resonance frequency of the membrane to measure the response of the same and also characterize the geometric non-linearity. In case when the PZT is turned off, the thermomechanical motion will generate sidebands on the pump signal at $\omega_d \pm \Omega_m$. The transmitted signal is then amplified and downconverted before measuring the signal with a lock-in amplifier using the zoom FFT method.

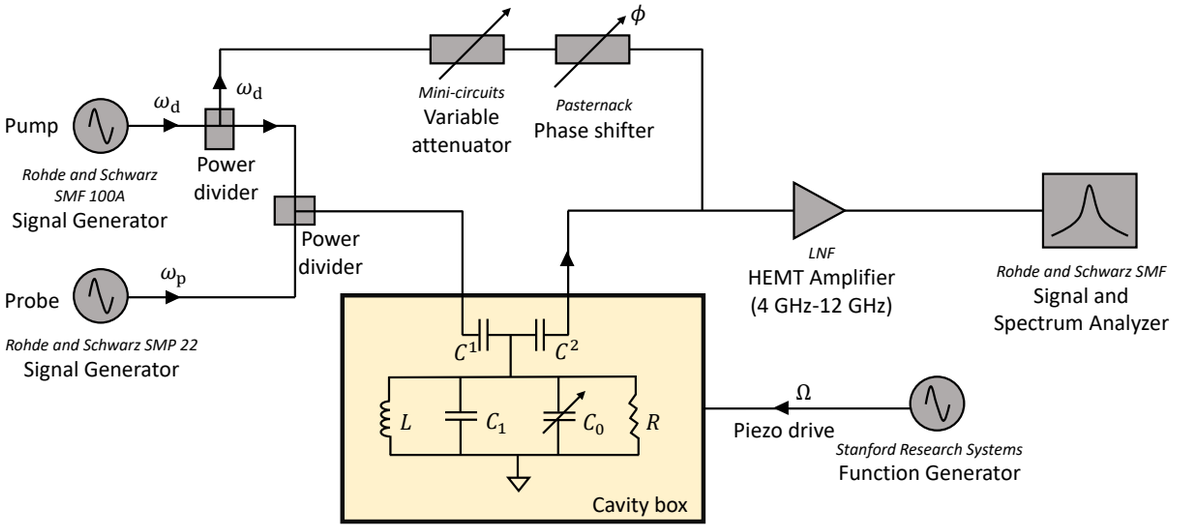

FIG. 8. Measurement circuit diagram for direct thermal noise spectral measurements, white noise driven spectral measurements and two-tone measurements. The signal was measured using the spectrum analyzer.

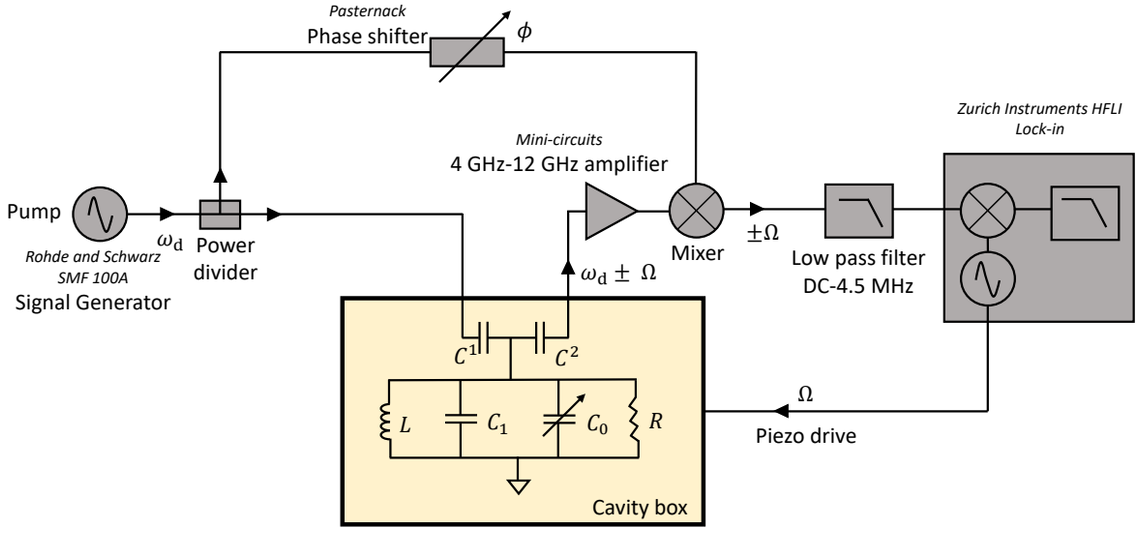

FIG. 9. Measurement circuit diagram for homodyne detection scheme. We used this circuit to measure the response of the periodically driven mechanical resonator and characterize the geometric non-linearity.

[1]D. Cattiaux, I. Golokolenov, S. Kumar, M. Sillanpää, L. Mercier de Lépinay, R. Gazizulin, X. Zhou, A. Armour, O. Bourgeois, A. Fefferman, *et al.*, Nature communications **12**, 1 (2021).
[2]J. D. Teufel, T. Donner, D. Li, J. W. Harlow, M. Allman, K. Cicak, A. J. Sirois, J. D. Whittaker, K. W. Lehnert, and R. W. Simmonds, Nature **475**, 359 (2011).
[3]J. Suh, A. Weinstein, C. Lei, E. Wollman, S. Steinke, P. Meystre, A. A. Clerk, and K. Schwab, Science **344**, 1262 (2014).
[4]C. Ockeloen-Korppi, E. Damskägg, J.-M. Pirkkalainen, A. Clerk, M. Woolley, and M. Sillanpää, Physical review letters **117**, 140401 (2016).
[5]C. Ockeloen-Korppi, E. Damskägg, J.-M. Pirkkalainen, M. Asjad, A. Clerk, F. Massel, M. Woolley, and M. Sillanpää, Nature **556**, 478 (2018).
[6]S. Kotler, G. A. Peterson, E. Shojaee, F. Lecocq, K. Cicak, A. Kwiatkowski, S. Geller, S. Glancy, E. Knill, R. W. Simmonds, *et al.*, Science **372**, 622 (2021).
[7]P. Weber, J. Güttinger, A. Noury, J. Vergara-Cruz, and A. Bachtold, Nature Communications **7**, 1 (2016).
[8]M. S. Hanay, S. Kelber, A. Naik, D. Chi, S. Hentz, E. Bullard, E. Colinet, L. Duraffourg, and M. Roukes, Nature nanotechnology **7**, 602 (2012).
[9]S. Kumar, D. Cattiaux, E. Collin, A. Fefferman, and X. Zhou, Journal of Low Temperature Physics , 1 (2022).
[10]F. Massel, T. T. Heikkilä, J.-M. Pirkkalainen, S.-U. Cho, H. Saloniemi, P. J. Hakonen, and M. A. Sillanpää, Nature **480**, 351 (2011).
[11]T. Clark, V. Vadakkumbatt, F. Souris, H. Ramp, and J. Davis, Review of Scientific Instruments **89**, 114704 (2018).
[12]S. Barzanjeh, M. Wulf, M. Peruzzo, M. Kalaee, P. Dieterle, O. Painter, and J. M. Fink, Nature communications **8**, 1 (2017).
[13]A. Schliesser, G. Anetsberger, R. Rivière, O. Arcizet, and T. J. Kippenberg, New Journal of Physics **10**, 095015 (2008).
[14]M. Sansa, M. Defoort, A. Brenac, M. Hermouet, L. Banniard, A. Fafin, M. Gely, C. Masselon, I. Favero, G. Jourdan, *et al.*, Nature Communications **11**, 1 (2020).
[15]E. Gavartin, P. Verlot, and T. J. Kippenberg, Nature nanotechnology **7**, 509 (2012).
[16]K. Srinivasan, H. Miao, M. T. Rakher, M. Davanco, and V. Aksyuk, Nano letters **11**, 791 (2011).
[17]P. E. Allain, L. Schwab, C. Mismer, M. Gely, E. Mairiaux, M. Hermouet, B. Walter, G. Leo, S. Hentz, M. Faucher, *et al.*, Nanoscale **12**, 2939 (2020).
[18]A. G. Krause, M. Winger, T. D. Blasius, Q. Lin, and O. Painter, Nature Photonics **6**, 768 (2012).
[19]H. J. Mamin, R. Budakian, B. W. Chui, and D. Rugar, Physical Review Letters **91**, 207604 (2003).
[20]R. A. Norte, J. P. Moura, and S. Gröblacher, Physical review letters **116**, 147202 (2016).
[21]A. Pearson, K. Khosla, M. Mergenthaler, G. A. D. Briggs, E. Laird, and N. Ares, Scientific reports **10**, 1 (2020).
[22]E. Serra, A. Borrielli, F. Marin, F. Marino, N. Malossi, B. Morana, P. Piergentili, G. A. Prodi, P. M. Sarro, P. Vezio, *et al.*, Journal of Applied Physics **130**, 064503 (2021).
[23]T. Faust, P. Krenn, S. Manus, J. P. Kotthaus, and E. M. Weig, Nature communications **3**, 1 (2012).
[24]M. Aspelmeyer, T. J. Kippenberg, and F. Marquardt, Reviews of Modern Physics **86**, 1391 (2014).
[25]A. T. Le, A. Brieussel, and E. M. Weig, Journal of Applied Physics **130**, 014301 (2021).
[26]Y. Liu, J. Zhou, L. M. de Lépinay, and M. A. Sillanpää, arXiv preprint arXiv:2201.11041 (2022).
[27]M. Yuan, V. Singh, Y. M. Blanter, and G. A. Steele, Nature communications **6**, 1 (2015).
[28]A. Noguchi, R. Yamazaki, M. Ataka, H. Fujita, Y. Tabuchi, T. Ishikawa, K. Usami, and Y. Nakamura, New Journal of Physics **18**, 103036 (2016).
[29]Anapol, `https://www.anapol.com/`.
[30]Twickenham plating group, `https://www.twickenham.co.uk/`.
[31]Norcada Inc., `https://www.norcada.com/`.
[32]B. Hauer, C. Doolin, K. Beach, and J. Davis, Annals of Physics **339**, 181 (2013).
[33]J. Cleveland, S. Manne, D. Bocek, and P. Hansma, Review of scientific instruments **64**, 403 (1993).
[34]S. Kumar, *Low temperature microwave optomechanics: anomalous force noise and optomechanically induced transparency*, Ph.D. thesis, Université Grenoble Alpes [2020-....] (2021).
[35]X. Zhou, D. Cattiaux, R. Gazizulin, A. Luck, O. Maillet, T. Crozes, J.-F. Motte, O. Bourgeois, A. Fefferman, and E. Collin, Physical Review Applied **12**, 044066 (2019).
[36]M. E. M. Pernpeintner, *Nanomechanical hybrid systems*, Ph.D. thesis, Technische Universität München (2016).
[37]M. Fleischhauer, A. Imamoglu, and J. P. Marangos, Reviews of modern physics **77**, 633 (2005).
[38]A. Schließer, *Cavity optomechanics and optical frequency comb generation with silica whispering-gallery-mode microresonators*, Ph.D. thesis, lmu (2009).
[39]S. Weis, R. Rivière, S. Deléglise, E. Gavartin, O. Arcizet, A. Schliesser, and T. J. Kippenberg, Science **330**, 1520 (2010).
[40]A. H. Safavi-Naeini, T. Alegre, J. Chan, M. Eichenfield, M. Winger, Q. Lin, J. T. Hill, D. E. Chang, and O. Painter, Nature **472**, 69 (2011).
[41]X. Zhou, S. Venkatachalam, R. Zhou, H. Xu, A. Pokharel, A. Fefferman, M. Zaknoune, and E. Collin, Nano Letters **21**, 5738 (2021).
[42]D. Cattiaux, S. Kumar, X. Zhou, A. Fefferman, and E. Collin, Journal of Applied Physics **128**, 104501 (2020).
[43]M. Gorodetksy, A. Schliesser, G. Anetsberger, S. Deleglise, and T. J. Kippenberg, Optics express **18**, 23236 (2010).
[44]H. Packard, Frequency Discriminator Method (1985).
[45]M. Goryachev and M. E. Tobar, Journal of Applied Physics **118**, 204504 (2015).
[46]"A novel architecture for room temperature microwave optomechanical experiments," `https://doi.org/10.5281/zenodo.7589222` (2023).
[47]C. Zhang, M. Giroux, T. A. Nour, and R. St-Gelais, Physical Review Applied **14**, 024072 (2020).

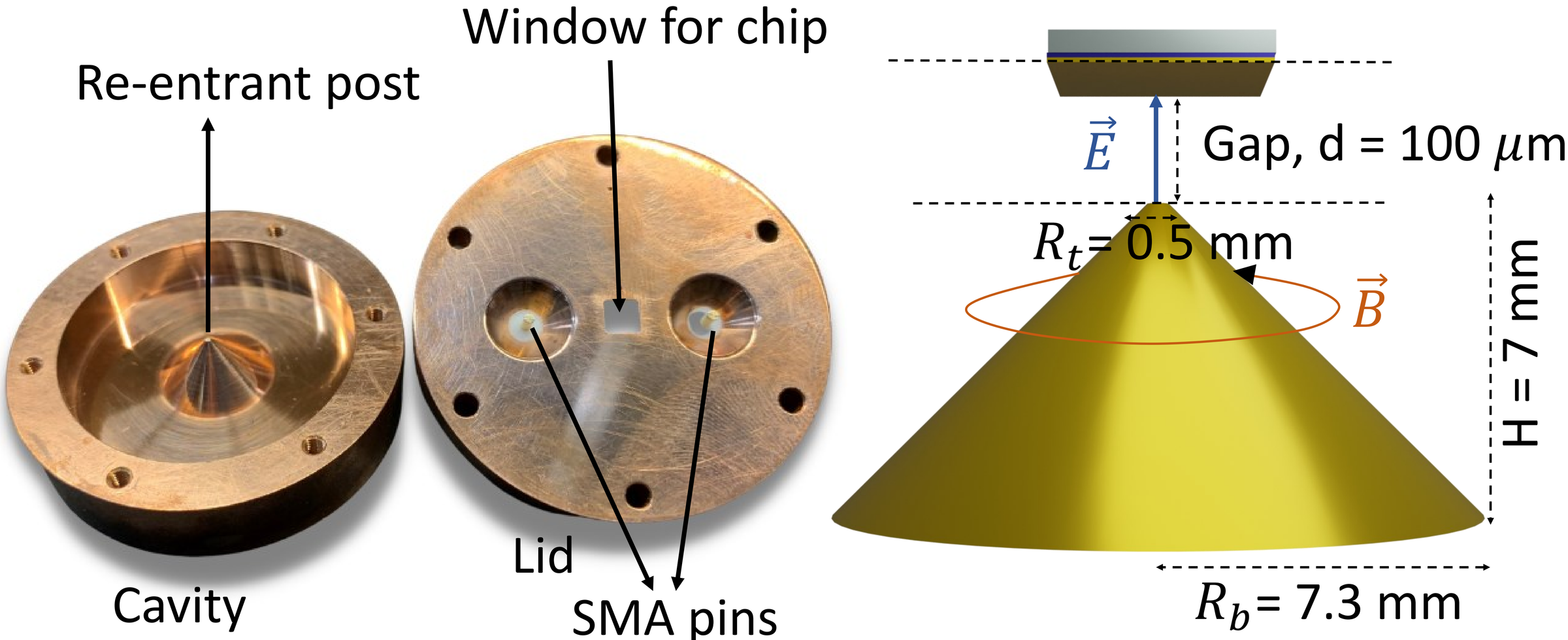

Journal of Applied Physics

AIP Publishing

Journal of Applied Physics

AIP Publishing

AIP Publishing

Journal of Applied Physics

ACCEPTED MANUSCRIPT

This is the author's peer reviewed, accepted manuscript. However, the online version of record will be different from this version once it has been copyedited and typeset.
PLEASE CITE THIS ARTICLE AS DOI: 10.1063/5.0136214

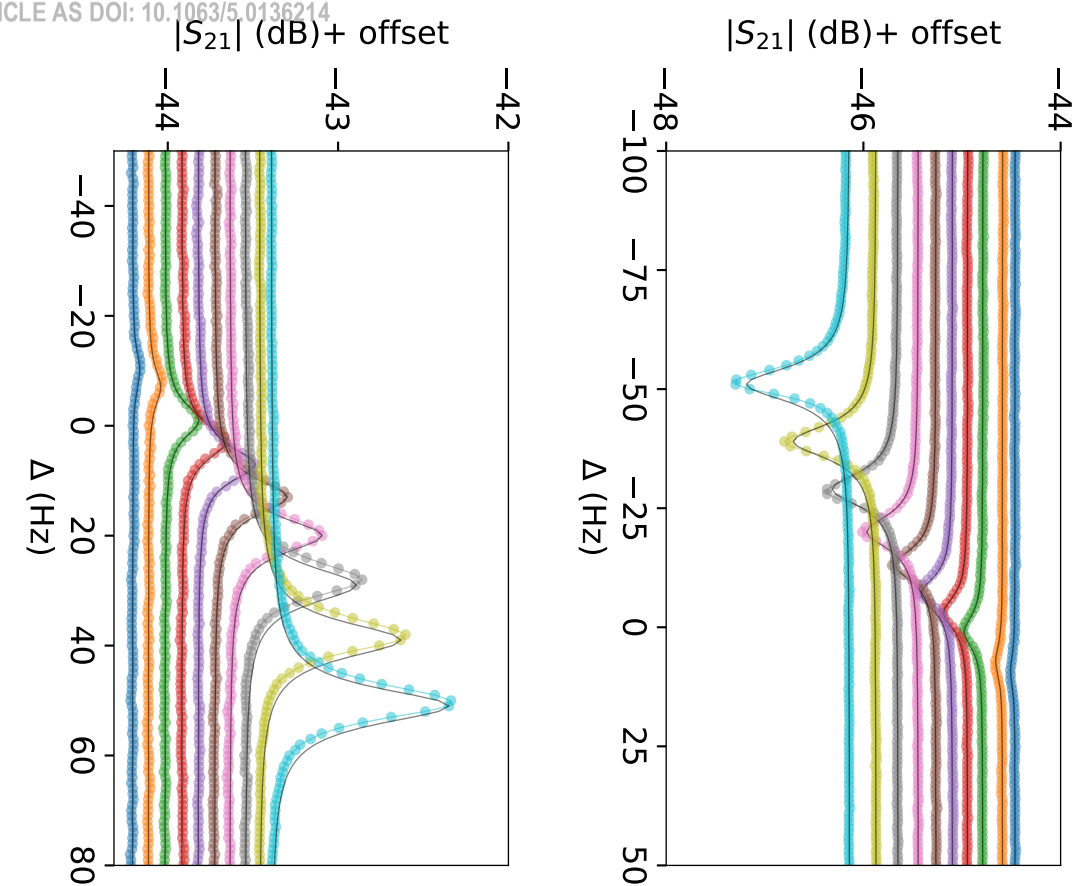

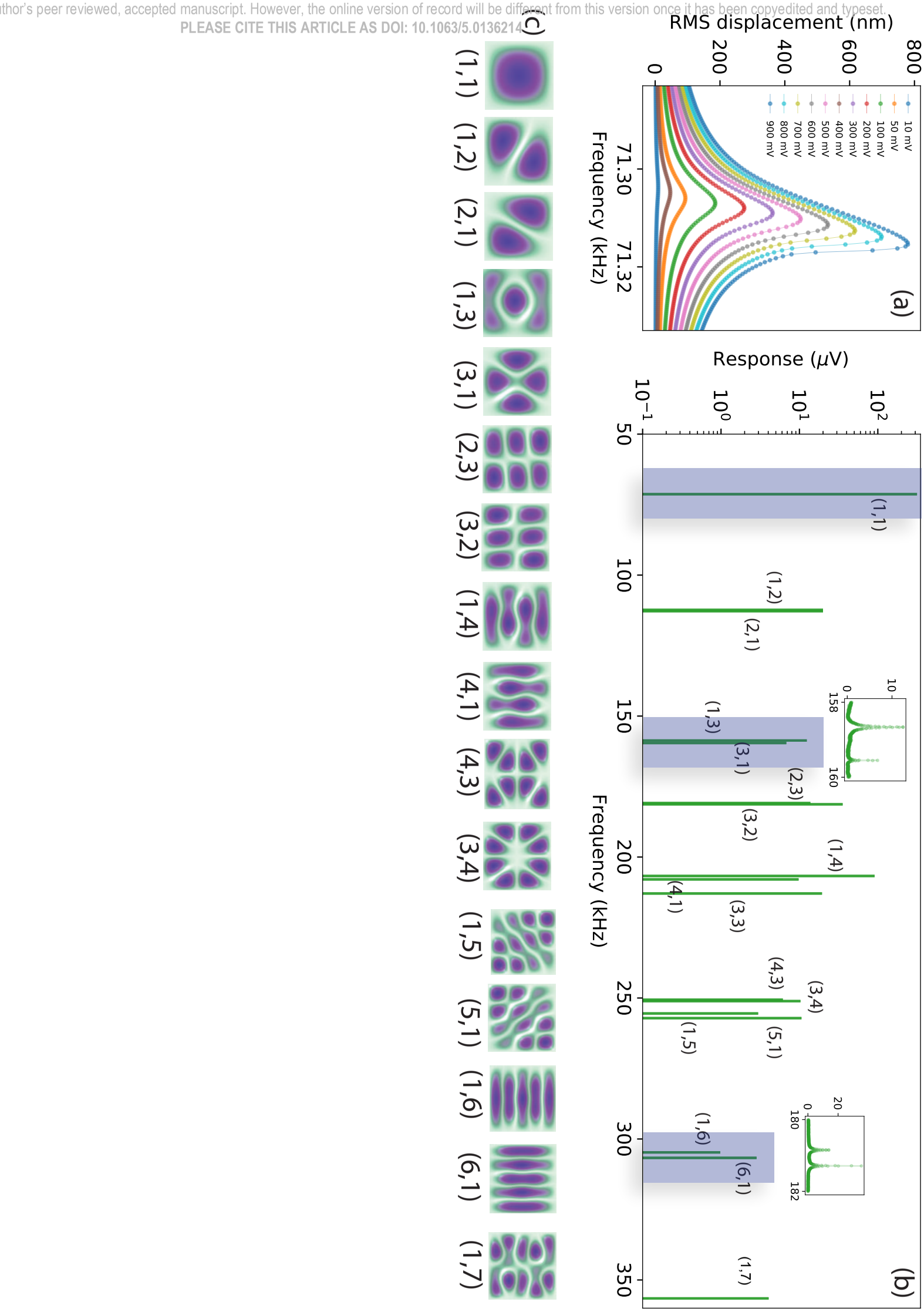

Journal of Applied Physics
AIP Publishing

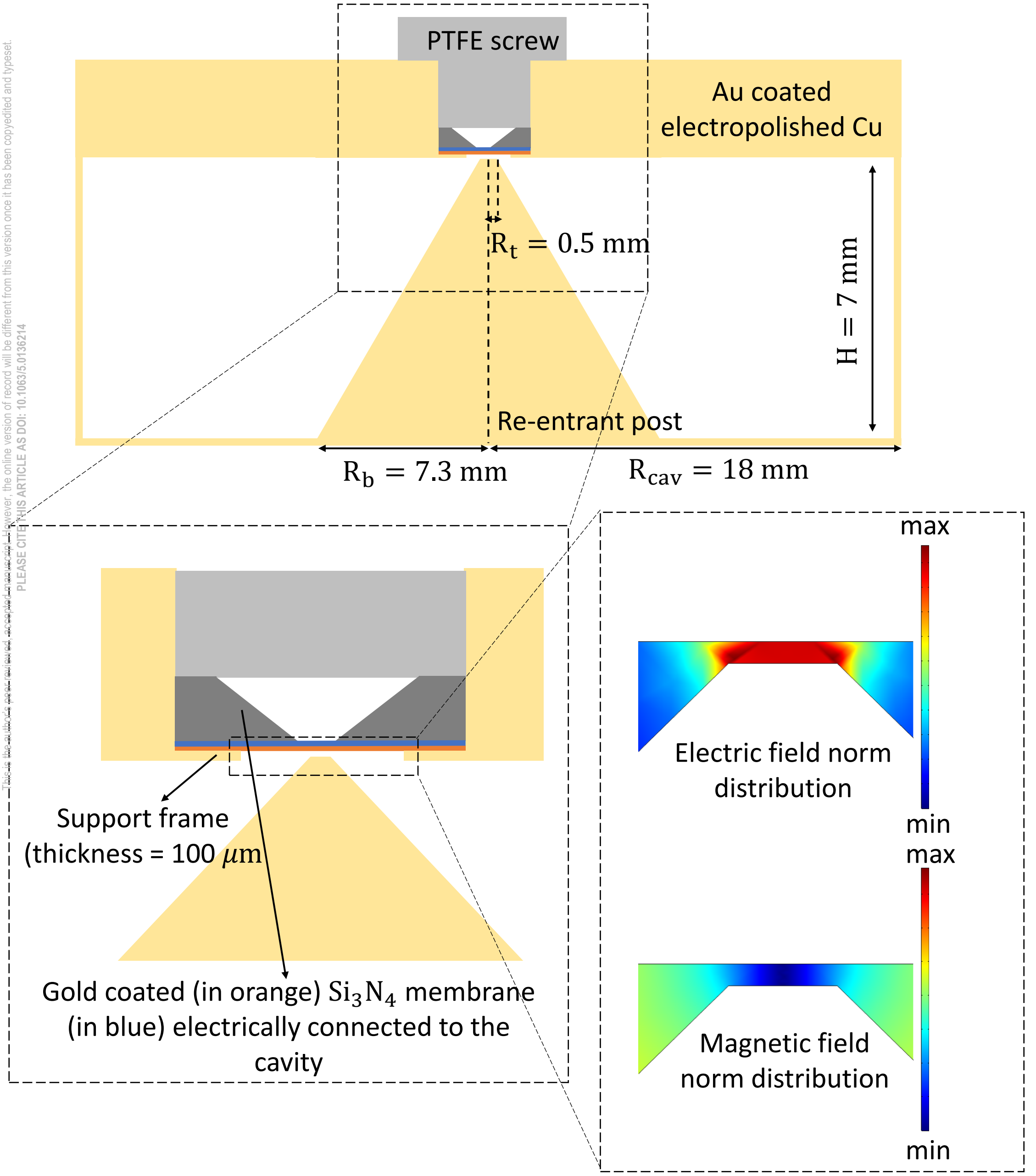

AIP Publishing

Journal of Applied Physics

ACCEPTED MANUSCRIPT

This is the author's peer reviewed, accepted manuscript. However, the online version of record will be different from this version once it has been copyedited and typeset.
PLEASE CITE THIS ARTICLE AS DOI: 10.1063/5.0136214

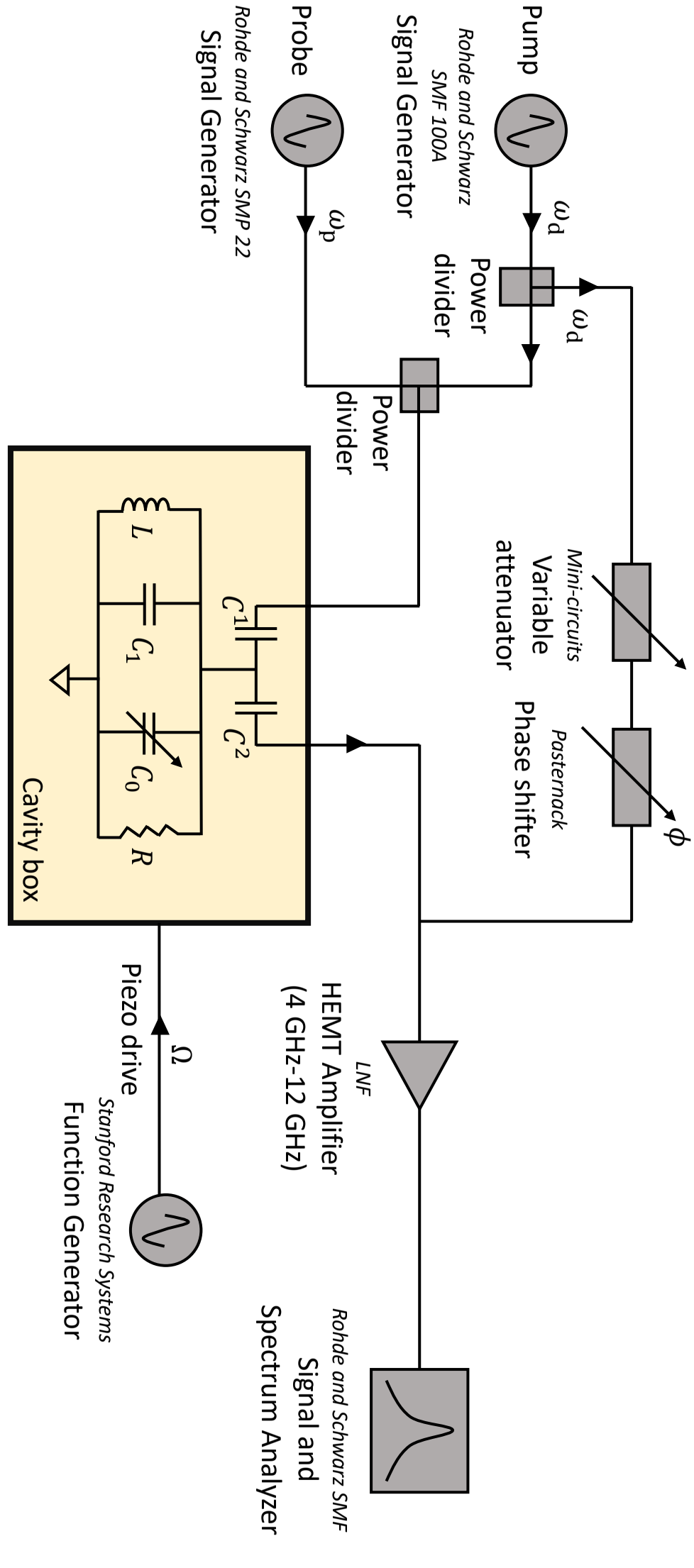

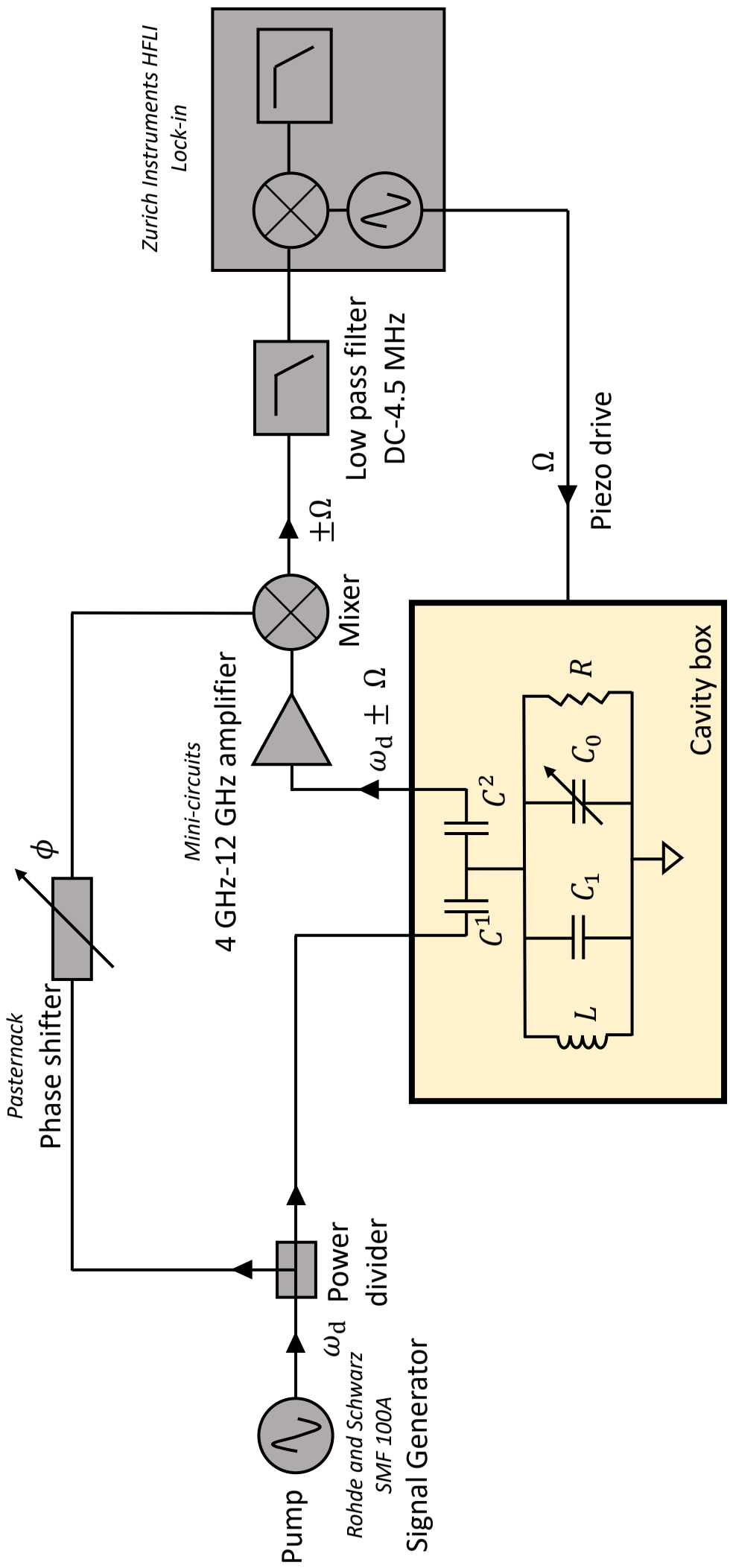

AIP Publishing

Journal of Applied Physics

ACCEPTED MANUSCRIPT

PLEASE CITE THIS ARTICLE AS DOI: 10.1063/5.0136214